Varactor-Based Frequency-Reconfigurable Dual-Polarized mm-Wave Antenna Array for Mobile Devices

Quangang Chen, Juha Ala-Laurinaho, Alexander Khripkov, *Member, IEEE*, Janne Ilvonen, Resti Montoya Moreno, and Ville Viikari, *Senior Member, IEEE*

***Abstract*— In this article, a dual-polarized frequency-reconfigurable mm-wave patch antenna array is described. The design incorporates varactor diodes (VDs) symmetrically loaded onto the four corners of a square patch. Parallel plate series capacitors are constructed to achieve the required low total capacitance by moving the square patch to an inner layer. Additionally, novel dual-function shorting vias are implemented into the structure, which serves as an RF choke for providing dc-bias voltage to the varactors and behave as shunt inductive loadings to improve radiation efficiency. A four-element antenna array is implemented and placed into a 21 × 4.5 mm^2 cavity. The proposed antenna array can be tuned from 23.2 to 30.2 GHz by adjusting the varactor capacitance from 0.22 to 0.033 pF. The array achieves over 20-dB isolation between the orthogonal-polarized antenna elements and more than 15-dB isolation between the same-polarized antenna elements. Total efficiency exceeds −2.5 dB across the tuning range. Peak gain varies from 8.9 to 10.5 dBi. The proposed dual-polarized antenna array offers notable advantages including a wide frequency-tuning range, high efficiency, compact size, and beam-forming capability.**

***Index Terms*— 5G, beam steering, dual polarized, mm-wave, multiple-input multiple-output (MIMO), patch antenna, reconfigurable antenna.**

I. Introduction

MOBILE communications have swiftly progressed from 1G to 5G to meet the burgeoning demand from the consumer market. The early stages of the 5G era predominantly focused on sub-6 GHz, employing multiple-input multiple-output (MIMO) techniques to enhance communication performance. Nevertheless, it confronts the same spectrum congestion challenge as the preceding 1G–4G technologies [1], [2], [3], [4]. Recently, the Third-Generation Partnership Project (3GPP) has divided the mm-wave spectrum into the following bands: n257 (26.5–29.5 GHz), n258 (24.25–27.5 GHz), and n261 (27.5–28.35 GHz) for 5G communications [5]. While mm-wave bands provide much greater bandwidths, several technical challenges need to be solved before their full potential can be exploited [6]. For example, beam-steerable arrays are needed on a mobile device to achieve good spherical gain coverage, and the antenna should operate in multiple frequency bands with minimal crosstalk among them.

In the past decades, there has been increased interest in reconfigurable antennas over fixed antennas among academia and industry. Reconfigurable antennas can be divided into four categories: 1) frequency reconfigurable [7], [8], [9], [10], [11]; 2) polarization reconfigurable [12], [13]; 3) radiation-pattern reconfigurable [14], [15]; and 4) different combinations of 1)–3) [16], [17]. These reconfigurable antennas have many advantages, e.g., wide frequency band in which they can operate, frequency-insensitive radiation properties, and small polarization mismatch. Although some broadband antennas can also achieve a sufficiently large bandwidth, it typically comes at a cost of electrically large antenna size and poor frequency selectivity. Frequency-reconfigurable antennas operate inherently as filters mitigating possible interference.

Compared to reconfigurable antenna designs at the sub-6 GHz range, it is more challenging to implement reconfigurable antenna concepts in the mm-wave spectrum. For instance, most of the commonly used tuning components are unusable at mm-wave frequencies where their self-resonance frequency is exceeded. Sufficiently high self-resonance frequencies and tolerable losses are needed. Another challenge is related to the electrical size of the tuning component. At mm-wave frequencies, tuning components can be electrically large and have a significant impact on radiated fields. As a result, achieving good performance with reconfigurable antennas in this spectrum, especially for consumer mobile devices with limited space, requires careful consideration of additional factors.

Although frequency-reconfigurable antennas have been extensively studied for frequencies in sub-6 GHz, they are rare in mm-wave bands due to the aforementioned challenges. The limited number of published antennas in this frequency range offer some degree of reconfigurability but not all of the necessary properties typically required for mobile device antennas. Because of the scarcity of available tunable components in the current market, more research in the mm-wave bands has been

Manuscript received 17 February 2023; revised 2 May 2023; accepted 24 May 2023. Date of publication 23 June 2023; date of current version 4 August 2023. This work was supported in part by Huawei Technologies Finland and in part by the Aalto ELEC Doctoral School. *(Corresponding author: Quangang Chen.)*

Quangang Chen, Juha Ala-Laurinaho, and Ville Viikari are with the Department of Electronics and Nanoengineering, School of Electrical Engineering, Aalto University, 00076 Espoo, Finland (e-mail: quangang.chen@aalto.fi).

Alexander Khripkov, Janne Ilvonen, and Resti Montoya Moreno are with Huawei Technologies Finland, 00180 Helsinki, Finland.

Color versions of one or more figures in this article are available at https://doi.org/10.1109/TAP.2023.3287679.

Digital Object Identifier 10.1109/TAP.2023.3287679

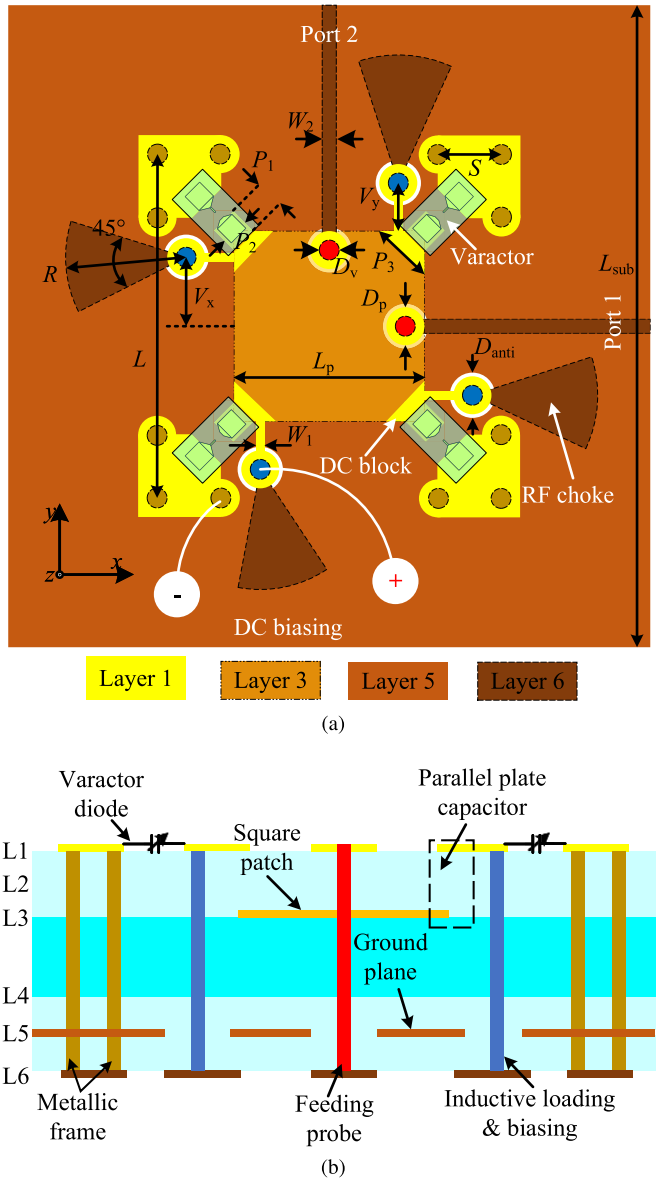

Fig. 1. Antenna element geometry. (a) Top view. (b) Stacked view.

focused on designing radiation pattern or/and polarization-reconfigurable antennas [18], [19], [20], and [21]. In [22] and [23], two resonant frequencies of the proposed antennas were adjusted by switching different matching circuits with a p-i-n diode. In addition to active components, continuous frequency tunability was realized with liquid crystals in [24]. In [25] and [26], frequency-reconfigurable antennas were achieved with photoconductive switches and paraffin materials, respectively. However, these solutions are not suitable for consumer electronics considering the antenna design environment. All the mentioned frequency-reconfigurable antenna designs were single polarized without beam-forming capability.

This article presents an mm-wave antenna array of large frequency tuning range, which is based on initial antenna element simulations reported in [27]. To the best of our knowledge, this is the first time that continuous frequency adjustment is achieved with high efficiency and dual

TABLE I
DIMENSIONS OF THE ANTENNA ELEMENT

Parameters	P_1	P_2	P_3	D_p	D_{anti}
Values(mm)	0.26	0.24	0.71	0.35	0.5
Parameters	D_v	L	W_1	W_2	L_{sub}
Values(mm)	0.15	3.25	0.1	0.12	20
Parameters	L_p	S	V_x	V_y	R
Values(mm)	1.8	0.5	0.73	0.4	1.5

polarization for 5G mm-wave consumer electronics. The corners of square patches are symmetrically loaded with VDs to achieve a large frequency tuning covering n257 (26.5–29.5 GHz), n258 (24.25–27.5 GHz), and n261 (27.5–28.35 GHz) of the mm-wave spectrum. The novelty of this work is that parallel plate series capacitors are constructed to decrease the total capacitance due to the scarcity of available low-capacitance VDs. In addition, inductive shorting vias are introduced close to varactors to reduce ohmic loss from the varactor's equivalent series resistance (ESR) when using a large capacitance value. Moreover, the bias circuits are implemented using the parallel plate capacitors and shorting vias to control the varactors, ensuring that there is no negative impact on performance. A 1 × 4 antenna array is built to demonstrate the frequency tunability and beam-forming capability in mm-wave frequency band.

II. DUAL-POLARIZED FREQUENCY-RECONFIGURABLE ANTENNA

A. Antenna Element Geometry

The proposed frequency-reconfigurable antenna configuration is shown in Fig. 1(a). The antenna element is constructed on a multi-layer printed circuit board (PCB) with six copper layers (from top to bottom), one core laminate, and four prepreg substrate layers as shown in Fig. 1(b). The 300-μm-thick laminate is R-5785N with relative permittivity $\epsilon_r = 3.34$ and loss tangent $\tan\delta = 0.003$, and the 60-μm-thick prepregs are R-5680N with $\epsilon_r = 3.14$ and $\tan\delta = 0.002$. The plated through holes (PTH) are drilled from the top layer to the bottom layer. Four right-triangle-shaped pads are etched on the top layer, and each pad is connected to the ground plane (L5) by three PTHs. A 1.8 ×1.8 mm^2 square patch on the third layer (L3) is located in the center of these four L-shaped metallic walls. Another four pads are placed on top of four corners of the square patch, and each of them connects with a $\lambda/4$ open radial stub printed on the bottom layer through a PTH. Two 50-Ω microstrip lines are used to feed the two orthogonal polarizations along x-axis and y-axis. Four VDs are diagonally mounted on the corners of the patch for symmetry. The anodes and cathodes of varactors are connected to the ground plane and open stubs, respectively, enabling individual biasing of each VD by applying a voltage between them. The specific dimensions are summarized in Table I.

Next, an available low-capacitance VD is employed to achieve the frequency reconfigurability. There are lots of commercial VDs working at sub-6 GHz, but few are suitable for mm-wave frequency bands [22]. The MAVR-011020-1411 from MACOM has a capacitance value as low as 0.025 pF

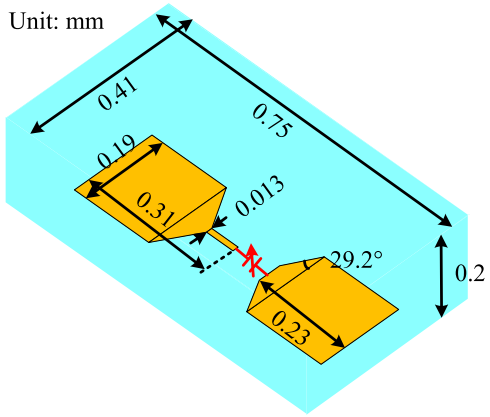

(a)

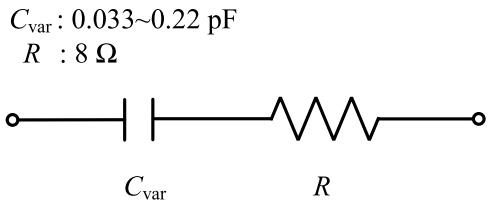

(b)

Fig. 2. VD model in simulations. (a) Three-dimensional model. (b) Equivalent circuit of the junction.

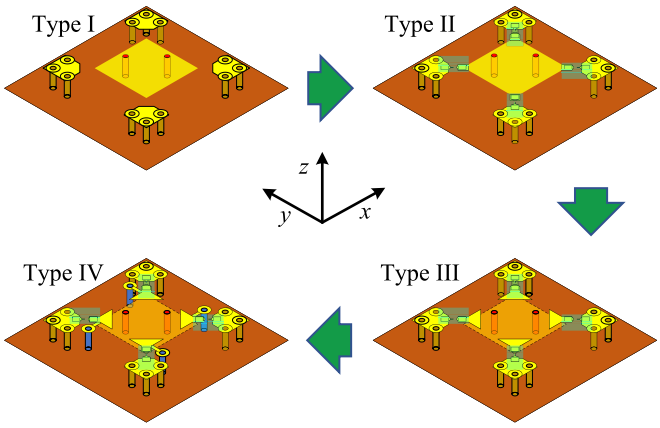

Fig. 3. Design procedure. Type I: original square patch. Type II: loading with VDs. Type III: adding parallel plate capacitors in series. Type IV: adding shorting vias.

and is used in this work [28]. Because the physical size of the VD is relatively large compared to the short wavelength at mm-wave frequency band, a 3-D VD model is built for accurate EM simulation as shown in Fig. 2(a). The effective material permittivity of the VD is $\epsilon_r = 6$ and loss tangent is $\tan\delta = 0.00056$ [29]. Fig. 2(b) gives an equivalent circuit which is used to characterize the junction of the VD in EM simulations. The capacitance range varies from 0.033 to 0.22 pF in the simulation, while the corresponding bias voltage decreases from 16 to 0 V.

B. Realization of Continuous Frequency Tunability

As shown in Fig. 3, a conventional dual-polarized square patch antenna (Type I) is first constructed to cover the mm-wave frequency bands n259 (39.5–43.5 GHz) and n260

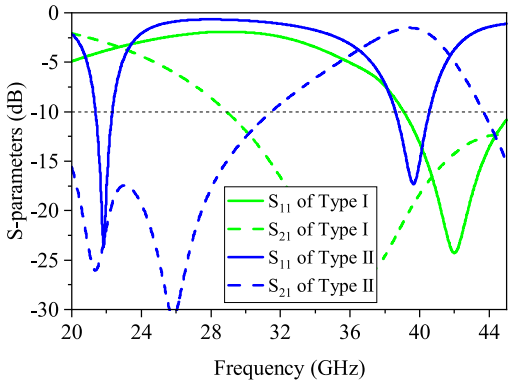

Fig. 4. Simulated S-parameters of Type-I and Type-II antennas.

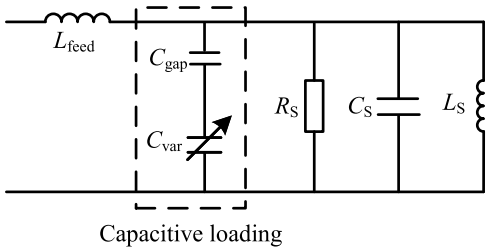

Fig. 5. Transmission line model of the VD-loaded patch antenna.

(37–40 GHz) using the following equation:

$$L_p = \frac{c}{2f\sqrt{(\varepsilon_r + 1)/2}} \tag{1}$$

and optimized in EM simulation. The corresponding S-parameters are plotted in Fig. 4. Because the structure is symmetrical with respect to the two polarizations, only S_{11} and S_{21} are displayed here. We know that a patch antenna can be characterized with a simplified RLC resonance circuit model as shown in Fig. 5, and the resonant frequency of the patch antenna will be decreased if an additional capacitance is loaded in parallel with C_s (capacitance of the patch) [30]. Based on [31], loading capacitors to the corners of the patch can maintain the original resonance and generate a new one in the low-frequency band. Besides, the symmetry of the structure should also be maintained to obtain good isolation between the two orthogonal polarizations. Therefore, four VDs are placed symmetrically between the metallic frames and the patch (Type II) to adjust the operating frequency as shown in Fig. 3. Accordingly, a new resonance is excited at 21.5 GHz when $C_{var} = 0.033$ pF (the smallest value) as depicted in Fig. 4, while the isolation performance is poor at high frequencies. Future work could aim to improve isolation and explore the potential for dual-band operation.

The Type-II antenna has a maximum operating frequency of 21.5 GHz due to the limitations of the available C_{var}. To cover the desired frequency range from 24 to 29.5 GHz, reducing the overall antenna aperture is one approach. However, this can lead to a significant decrease in efficiency caused by high power dissipation on the varactors. Our simulation shows that the radiation efficiency can drop as low as −5 dB when the antenna is shrunk ($L = 2$ mm, $L_p = 0.85$ mm). Another approach is to decrease the capacitance further.

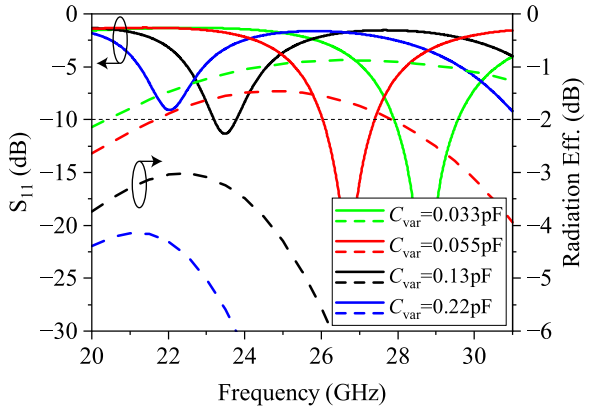

Fig. 6. Simulated performance of Type-III antenna with various C_{var} values. Solid lines for reflection coefficients and dashed lines for radiation efficiencies.

From the following equation:

$$\frac{1}{C_{tot}} = \frac{1}{C_{var}} + \frac{1}{C_{gap}} \tag{2}$$

we know that the total capacitance C_{tot} can be reduced by connecting a series capacitor C_{gap} as illustrated in Fig. 5. Nevertheless, the capacitance value of the VD still should be small enough to obtain a large tuning range based on (2). The operating frequency band can be first shifted to the desired range easily by adjusting the series C_{gap}, after which continuous frequency tuning can be achieved by controlling C_{var} of varactors to cover the entire frequency band of interest. The frequency-reconfigurable antenna is still electrically tuned by controlling the bias voltage.

To avoid introducing additional loss, coupling structures are utilized as distributed capacitors rather than lumped ones. The process of creating edge capacitors by etching narrow slits on the square patch poses challenges due to the required narrow gap and the limitations of standard PCB manufacturing tolerances. To address this issue, the square patch is relocated to Layer 3 (Type III), as depicted in Fig. 3, and parallel plate capacitors are formed between the patch and varactor's soldering pads on top layer. This approach offers a more convenient way to obtain the required capacitance by controlling the surface area of the plates and/or the distance between them. Fig. 6 demonstrates the corresponding S-parameters after loading series capacitors. It can be seen that the resonant frequencies are shifted successfully to the target range from 28.7 to 22 GHz as C_{var} varies from 0.033 to 0.22 pF.

C. Antenna Efficiency Improvement and Bias Circuit

However, the antenna efficiency is deteriorated dramatically due to the high power dissipation on the VDs (ESR = 8 Ω). The radiation efficiency at 23.5 GHz is only −3.3 dB when C_{var} = 0.13 pF as shown in Fig. 6. In order to increase the antenna efficiency, inductive loadings are introduced to compensate for the power dissipation on the varactors. As shown in Fig. 3, four shorting vias are symmetrically added to the corners of the square patch (Type IV). The cathode pads of the varactors are connected to the ground plane directly by these shorting vias.

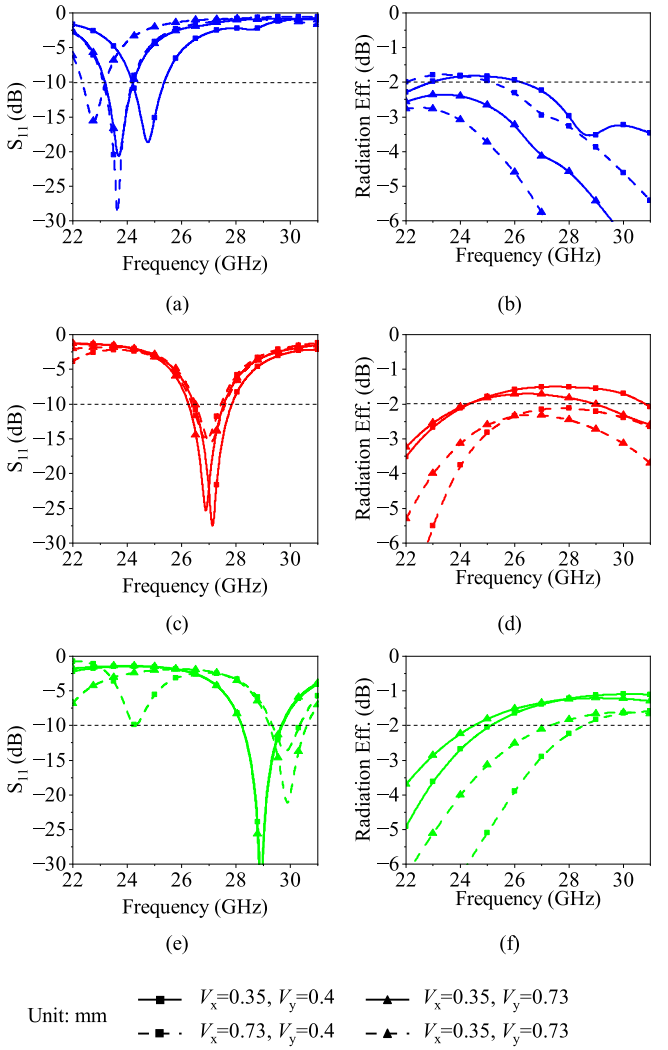

Fig. 7. Loading effects of shorting vias in Type-IV antenna at different via locations on reflection coefficient and radiation efficiency when (a) and (b) C_{var} = 0.22 pF, (c) and (d) C_{var} = 0.055 pF, and (e) and (f) C_{var} = 0.033 pF.

To illustrate the impacts of shorting vias, different locations of shorting vias in Type-IV antenna are studied as shown in Fig. 7. The resonant frequencies shift to the higher frequency in varying degrees as depicted in Fig. 7(a), (c), and (e) when compared with those of Type-III antenna in Fig. 6 [32]. It can be observed that the impedance bandwidth is increased with larger values of offset V_x (i.e., the larger the offset, the wider the bandwidth). Additionally, a significant impact on the resonance at lower frequencies is exerted by the distance V_y, where larger frequency shifts are produced with smaller values of V_y when compared to those of the Type-III antenna depicted in Fig. 6. More importantly, significant efficiency improvement can be observed at low frequency after loading shorting vias as depicted in Fig. 7(b). The radiation efficiency of Type IV can be improved by 1.5 dB at 23.5 GHz compared with that of Type-III antenna with C_{var} = 0.13 pF (see Fig. 6). For this study, V_x = 0.73 mm and V_y = 0.4 mm are selected for experimentation to achieve a broader operating bandwidth, despite a reduction in efficiency at high frequencies compared

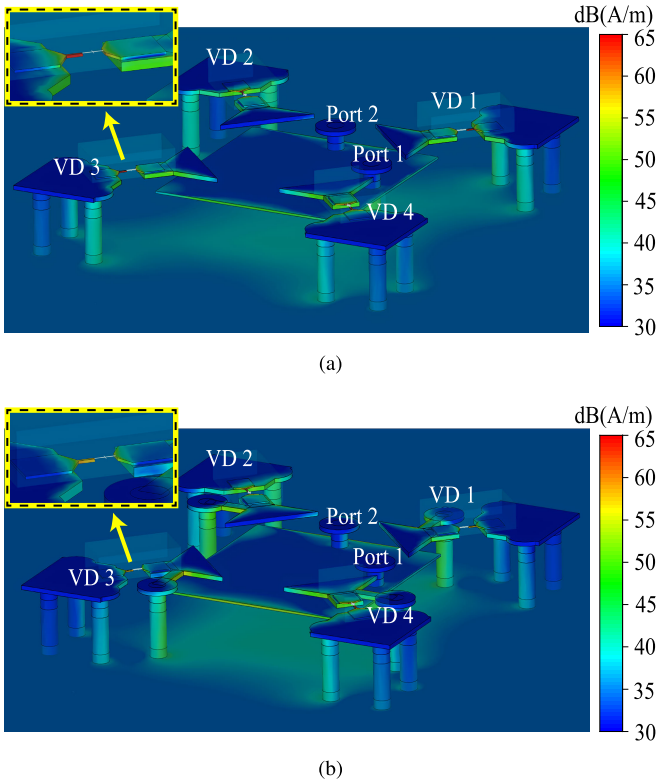

Fig. 8. Simulated current distributions for (a) Type-III and (b) Type-IV antennas resonating at 23.5 GHz, respectively, when Port 1 is excited. (c) Corresponding current strengths flowing through four VDs.

to $V_x = 0.35$ mm and $V_y = 0.4$ mm. It is noteworthy that the array-realized gain is also a consideration when selecting the location of the shorting via.

The current distributions at 23.5 GHz are plotted in Fig. 8(a) and (b) when C_{var} is 0.13 and 0.22 pF for Type-III and Type-IV antennas, respectively. The corresponding current strength flowing through four VDs are demonstrated in Fig. 8(c) for the two antenna types. It can be seen that strong currents flow through the four VDs in Type-III antenna. However, upon the addition of shorting vias, the current dramatically decreases, particularly in VDs 1 and 3. Therefore, the ohmic loss in the VDs is reduced. The VD can be seen as a straight-through circuit with a resistor when working at high-capacitance states. In this regard, the shorting via, functioning

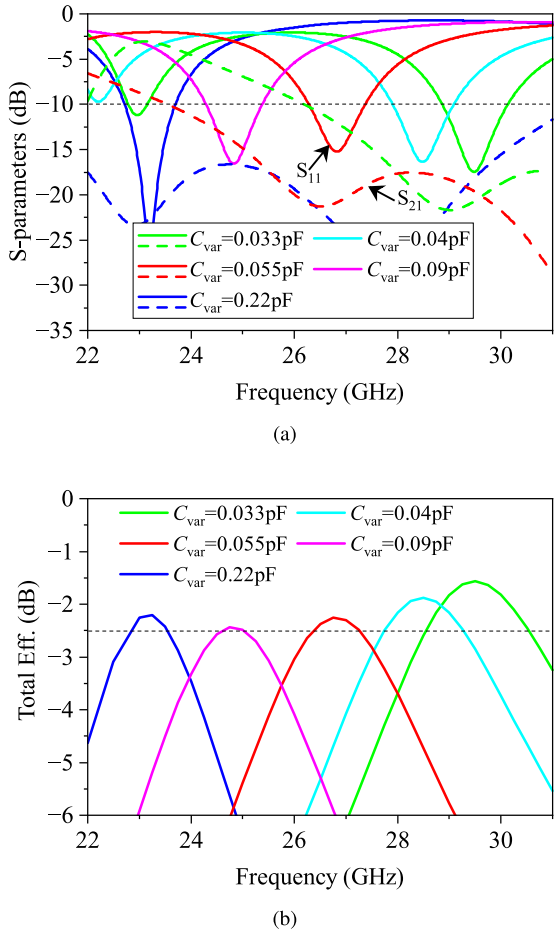

Fig. 9. Simulated performance of proposed antenna element. (a) S-parameters. (b) Total efficiencies.

as a shunt inductor without any resistance, can diminish the current flowing through the VD. Although this may undermine the VD's frequency adjustment capability, it significantly improves antenna efficiency. Besides, the shunt inductor is of higher impedance, reducing its impacts at high frequencies. By strategically selecting the shorting via's placement, adequate bandwidth can still be maintained.

Another advantage of the shorting vias is their easy modification to act as bias circuits for the corresponding varactors. It is well known that shorting circuit can be replaced with a quarter-wavelength open circuit in radio wave technology. Accordingly, a $\lambda/4$ open radial stub of wide bandwidth is designed to act as a virtual grounded point for the shorting via. The $\lambda/4$ open radial stub is an RF choke allowing for the addition of dc controlling lines after it. As for the dc block, the parallel plate capacitor can naturally play this role to block the dc signal. Therefore, the complete bias circuit is realized by utilizing the features of antenna structure, thereby avoiding any parasitics introduced from additional bias circuitry.

D. Performance of the Proposed Antenna Element

The dual-polarized frequency-reconfigurable antenna element is designed by conducting above-mentioned analysis as shown in Fig. 1. The S-parameters of the proposed antenna element are given in Fig. 9(a). The simulated results demonstrate

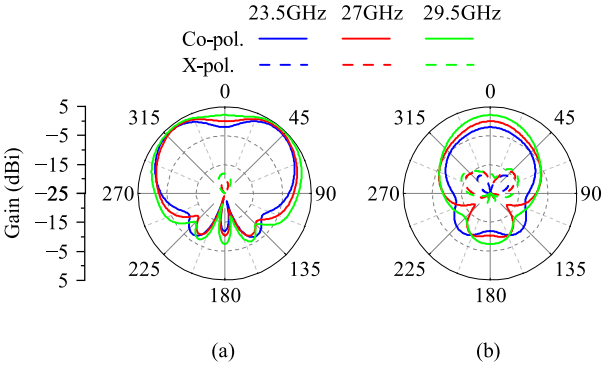

Fig. 10. Simulated radiation patterns of port 1 at different frequencies in (a) *xoz*-plane and (b) *yoz*-plane.

a frequency tuning from 30.2 to 22.7 GHz when C_{var} increases from 0.033 to 0.22 pF, and the isolations between the two feeding ports are greater than 20 dB in the corresponding operating frequencies. High total efficiencies are maintained across the entire frequency band as demonstrated in Fig. 9(b).

The simulated radiation patterns of antenna element at 23.5, 27, and 29.5 GHz are plotted in Fig. 10 when the C_{var} values are 0.22, 0.055, and 0.033 pF, respectively. As the frequency increases, the peak gain increases from 3.6 to 4.6 dBi. The cross-polarization levels are 20 dB lower than the co-polarization in both E- and H-planes. A dip in the broadside direction can be observed because of the loadings at four corners of the antenna element.

E. Four-Element Antenna Array

The dual-polarized frequency-reconfigurable antenna element has been optimized to cover the entire desired frequency band with high efficiency. Based on the antenna element, a 1 × 4 antenna array is designed to achieve beamforming in mm-wave frequency band. A 21 × 4.5 mm^2 cavity is constructed using a via fence, and the proposed antenna array is placed inside it, with an element spacing of 5.5 mm. The antenna elements are rotated 45° to easily facilitate routing of the feeding lines and biasing lines as shown in Fig. 11. The performance of the antenna array with non-rotated elements is comparable in terms of S-parameters and spherical coverage. The same stack up as shown in Fig. 1(b) is used in the array configuration. The antenna geometry is highlighted in Fig. 11(b). In addition, 50-Ω microstrip lines are placed within a 1-mm-wide gap and extended for the connection with vertical launch connectors. The 1 × 4 antenna array has four ports for each polarization, with ports 1, 3, 5, and 7 for +45° polarization and ports 2, 4, 6, and 8 for −45° polarization. Solder masks are printed on the top layer to guide the soldering of the flip chip VDs, and 1000-Ω resistors are mounted on the bottom to protect the VDs. DC biasing lines start from the virtual shorting point of the $\lambda/4$ open radial stub, go through the resistors, and end at the soldered headers for the anode. The cathode is soldered directly to the bottom.

Fig. 12 demonstrates the simulated S-parameters of the proposed array. Because of its symmetrical structure, the reflection coefficients of ports 1–4 are plotted in Fig. 12(a)

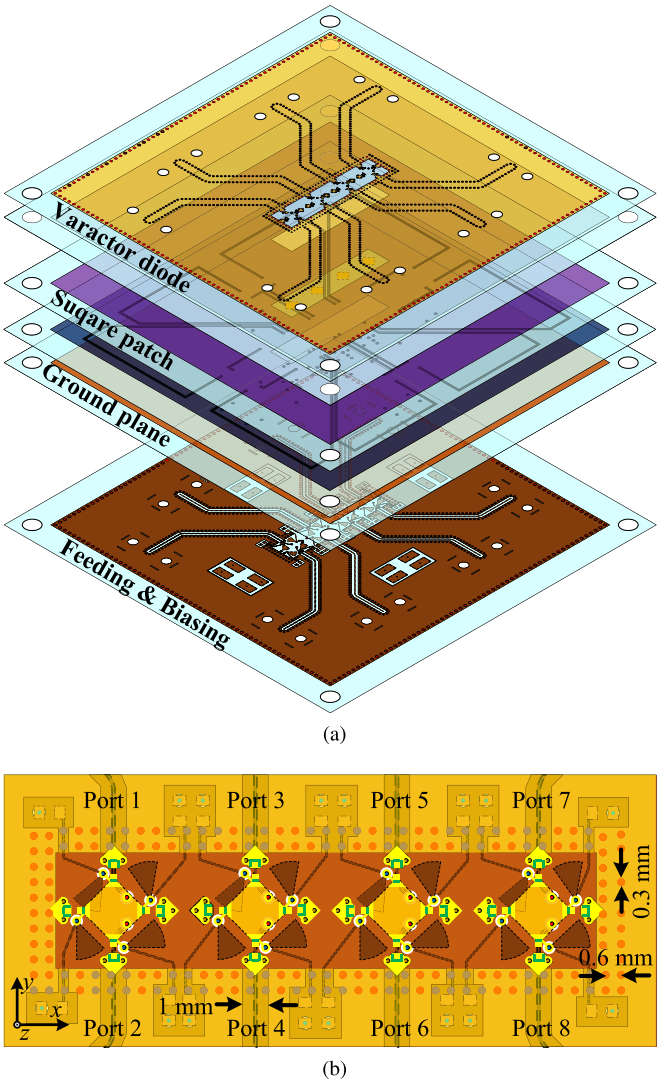

Fig. 11. Antenna array geometry. (a) Exploded view. (b) Perspective view.

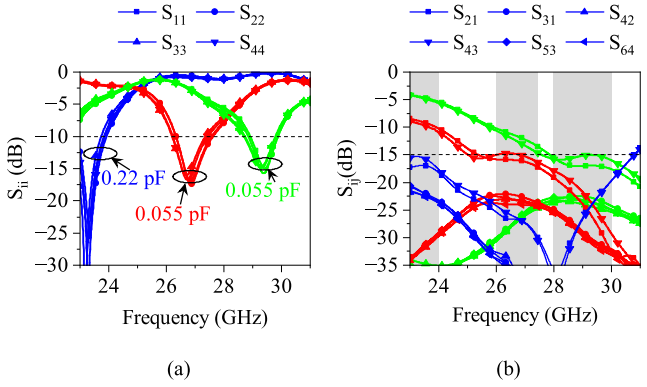

Fig. 12. Simulated S-parameters of the proposed antenna array for three working states: C_{var} = 0.22 pF, C_{var} = 0.055 pF, and C_{var} = 0.033 pF. (a) Reflection coefficients. (b) Transmission coefficients.

for brevity. It can be seen that the operating frequency band of the dual polarization can cover 28–30 GHz, 26–27.5 GHz, and 23–24 GHz with a −10 dB return loss when C_{var} = 0.033, 0.055, and 0.22 pF, respectively. The full frequency band of interest can be achieved with precise tuning of

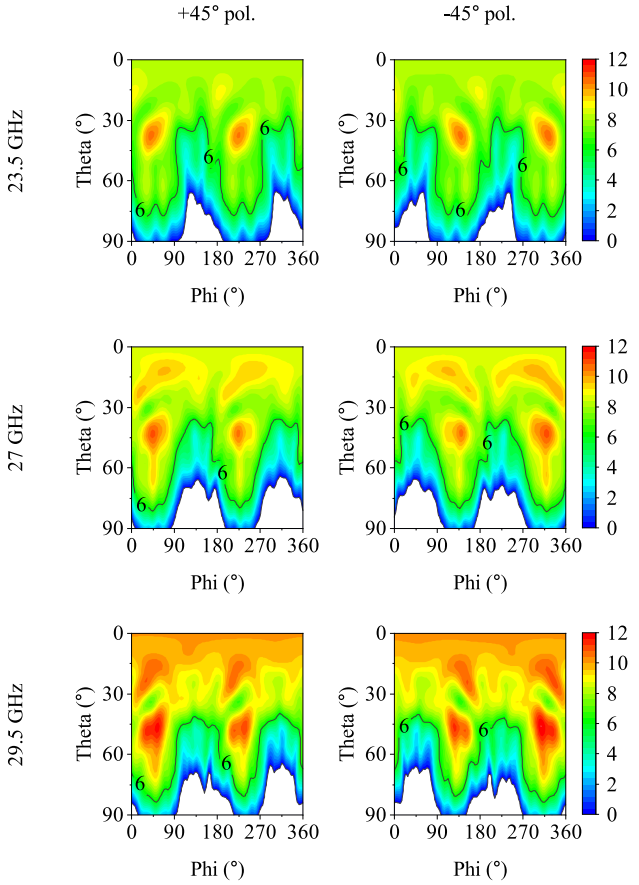

Fig. 13. Simulated total scan patterns of the maximum realized gain.

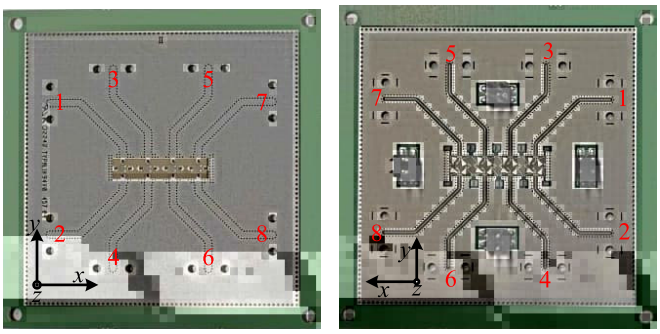

(a) (b)

Fig. 14. Fabricated antenna array prototype. (a) Top view. (b) Bottom view.

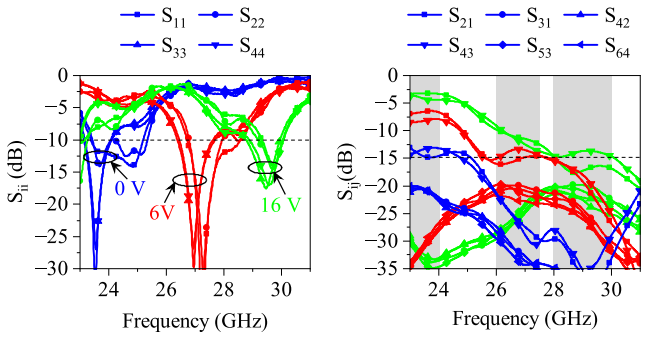

(a) (b)

Fig. 15. Measured S-parameters of the proposed antenna array for three working states: $V_{\text{bias}} = 0$ V, $V_{\text{bias}} = 6$ V, and $V_{\text{bias}} = 16$ V. (a) Reflection coefficients. (b) Transmission coefficients.

varactors. The isolations among array elements are shown in Fig. 12(b). The substantial isolation within the array constitutes another benefit of the proposed design. This high isolation is attained through a symmetrical antenna structure, which ensures 20-dB isolation between orthogonally polarized feeding ports. Furthermore, the 5.5-mm center-to-center distance between adjacent elements (equivalent to half the wavelength at 27 GHz) sufficiently provides a 15-dB isolation level between same polarized feeding ports.

Two-dimensional total scan patterns at selected frequencies show the maximum array gains with optimized feed coefficients towards all angles of the hemisphere ($+z$), as presented in Fig. 13. Because of the rotated antenna element and ground effect, peak gain of steered beams for the dual polarization is realized in the $\varphi = 45°$ cut and $\varphi = 135°$ cut, respectively.

III. Fabrication and Measurement

A. Antenna Fabrication

A prototype of the dual-polarized frequency-reconfigurable antenna array is fabricated based on the simulated design. Sixteen varactors are attached with flip-chip technique. Four headers and 16 resistors are also soldered on reserved pads. The photos of assembled prototype are shown in Fig. 14. The eight ports are numbered as they are in the simulated model.

B. S-Parameters

The S-parameters of the fabricated prototype are measured with a vector network analyzer (VNA). The measured S-parameters of three different working states are shown in Fig. 15. The antenna array prototype is resonant at 23.5, 27, and 29.5 GHz when the bias voltages V_{bias} are 0, 6, and 16 V, respectively. By adjusting the corresponding bias voltages, the measured impedance bandwidth of the proposed frequency-reconfigurable antenna array ranges from 23.2 to 30.2 GHz with a reflection coefficient smaller than -10 dB. In addition, the array exhibits high levels of isolation among its antenna elements in the corresponding operating frequency bands, with the lowest isolation level being greater than 13 dB at 23.5 GHz.

The measurement results are in good agreement with the simulation ones (see Fig. 12). The results of antenna elements located on the side of the array (i.e., ports 1, 2, 7, and 8) shift to high frequency slightly, and another resonance is observed at low frequencies when bias voltage is 0 V. The differences between the simulated and measured performance are primarily attributed to the manufacturing and assembly tolerances.

C. Radiation Patterns

The radiation patterns of the proposed antenna array are measured in an anechoic chamber port by port, while the remaining ones are terminated to 50-Ω loads. Element patterns of ports 1–4 at 27 GHz are presented in Fig. 16 for brevity. Since all antenna elements are rotated 45°, the E-plane and H-plane of ports 1 and 3 are along $\varphi = 45°$ and $\varphi = 135°$ cuts, respectively, and vice versa for ports 2 and 4. The measured

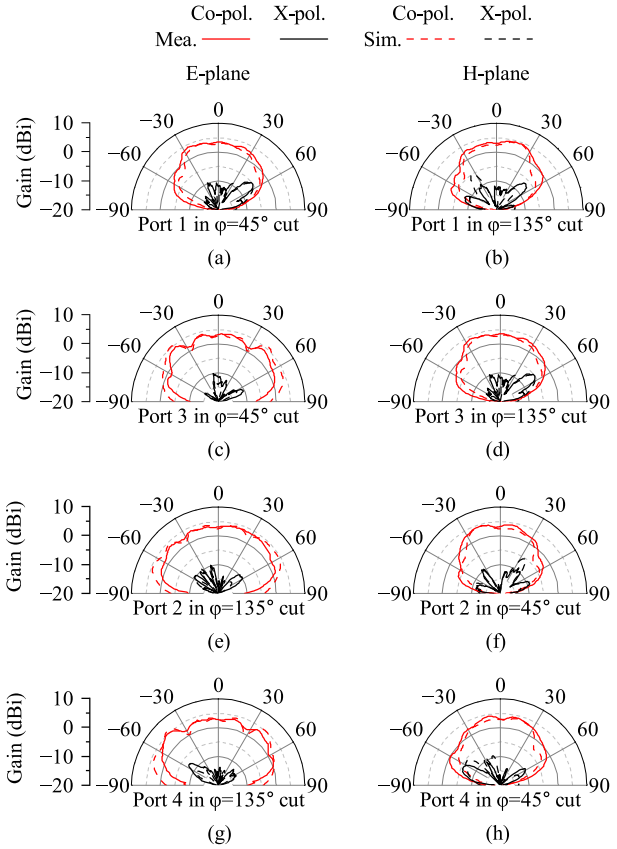

Fig. 16. Simulated and measured radiation patterns of ports 1–4 in E- and H-planes at 27 GHz.

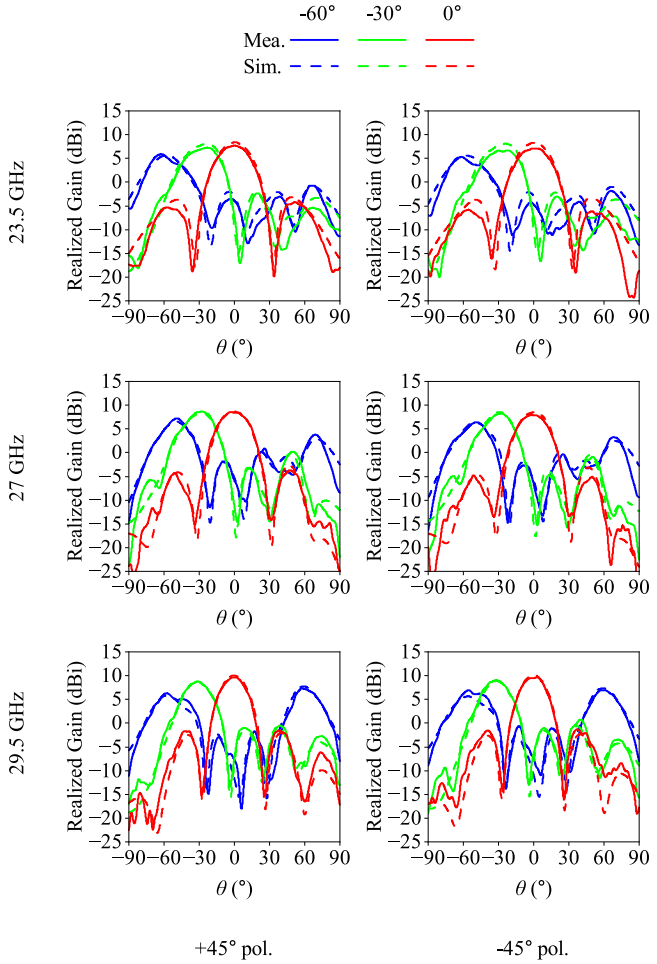

Fig. 17. Beam-steering performance of the proposed antenna array at different frequencies.

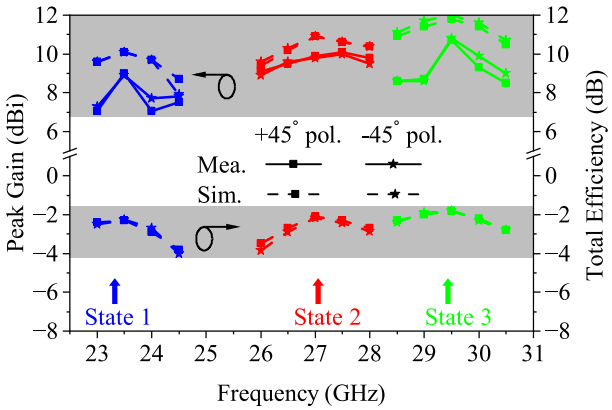

Fig. 18. Simulated and measured peak gains and simulated total efficiencies of the proposed antenna array at different working states. State 1: $C_{var} = 0.22$ pF or $V_{bias} = 0$ V. State 2: $C_{var} = 0.055$ pF or $V_{bias} = 6$ V. State 3: $C_{var} = 0.033$ pF or $V_{bias} = 16$ V.

radiation patterns are narrower in the E-plane and wider in the H-plane compared to the simulated patterns. The difference between simulated and measured radiation at large angles is from the measurement setup and fabrication tolerances. The dual-polarization feature of the array is symmetrical, leading to comparable radiation characteristics between the antenna elements on the side (ports 1 and 2), and those in the middle (ports 3 and 4) of the array.

The beam-forming capability of the mm-wave antenna array is calculated using the measured element radiation patterns. The steered beams towards $\theta = -60°, -30°$, and $0°$ are synthesized at 23.5, 27, and 29.5 GHz, as shown in Fig. 17. The measured scanned beams match well with the simulated ones. Stable radiation patterns are maintained across the frequency band. As the array scans to large angles, the grating lobes become increasingly prominent at 29.5 GHz due to the relatively large element spacing. However, the array gain remains above 5.2 dBi across the desired frequency band when scanning to $-60°$. Fig. 18 compares the simulated and measured peak realized gains of the proposed antenna array at different working states. It can be seen that the measured peak array gains are 8.9, 10, and 10.5 dBi at 23.5, 27, and 29.5 GHz, respectively. The differences between the measured and simulated peak gains can be attributed to factors such as the measurement setup and potential fabrication errors. In Figs. 13 and 19, it can be observed that the simulated peak gains occur at large theta angles, whereas the measured gains are comparatively lower in that range. This difference can be partially explained by the slight variations in the element patterns (refer to Fig. 16) at larger angles, which are influenced by practical implementation and measurement setup factors, such as shadowing of the absorbers close to the antenna. The lower part of Fig. 18 displays the simulated total efficiencies. The total efficiency varies from -2.3 to -1.8 dB across the

TABLE II
COMPARISON BETWEEN PROPOSED DESIGN AND REFERENCES

Ref.	[9]	[18]	[20]	[22]	[24]	[25]	**This work**
Reconfigurable parameters	Frequency	Pattern	Polarization	Frequency	Frequency	Frequency	**Frequency**
Active components	Varactor diodes	PIN diodes	PIN diodes	PIN diodes	Liquid crystals	Photoconductive switches	**Varactor diodes**
Working states	Continuous	3	2	2	Continuous	2	**Continuous**
Frequency range	0.6–1 GHz (50 %)	24–27.5 GHz (13.6 %)	27.2–28.35 GHz (4.1 %)	27.95–28.65 GHz (2.5 %)	27–30.5 GHz (12.2 %)	27.6–30.8 GHz (12.3 %) 36.8–38.4 GHz (4.3 %)	**23.2–30.2 GHz (26.2 %)**
Antenna configuration	1	1×4	$4^{\#}$	$4^{\#}$	1	$4^{\#}$	**1×4**
Antenna size	$0.27\times0.27\ \lambda_0^{2*}$	$1.8\times0.34\ \lambda_0^2$	$1.39\times1.39\ \lambda_0^2$	$1.9\times0.29\ \lambda_0^2$	$0.53\times0.35\ \lambda_0^{2*}$	$4.77\times0.55\ \lambda_0^2$	$\mathbf{1.87\times0.4\ \lambda_0^2}$
Polarization	Dual	Single	Dual	Single	Single	Single	**Dual**
Peak gain	-2.2–4.5 dBi*	5.3–10.7 dBi	4.5–7 dBi	4.8–6.1 dBi	3.9 dBi*	8–9 dBi	**8.9–10.8 dBi**
Total efficiency	21–72 %*	68–80 %	50 %	NA	78–83 %*	NA	**60–70 %**
Scalability^{+}	Yes	Yes	Yes	Yes	No	No	**Yes**

$^{\#}$: no beam–forming capability.

* : refers to element performance.

$^{+}$: refers to the ability of the manufacturing process to produce a large quantity of PCBs efficiently, consistently and cost-effectively.

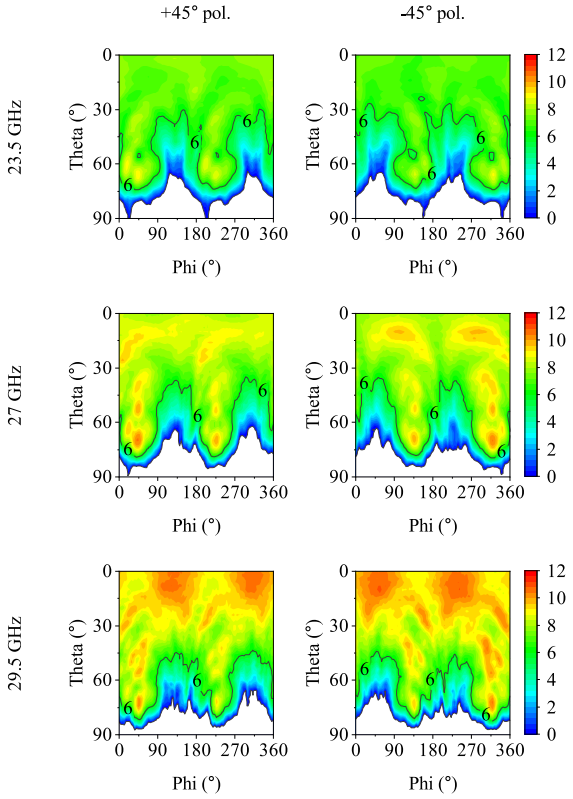

Fig. 19. Measured total scan patterns of the maximum realized gain.

whole frequency band. As the simulated and measured realized gains are in good agreement, the measured total efficiencies are expected to be comparable to the simulated values.

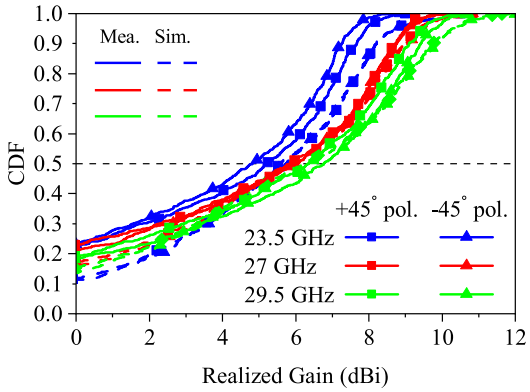

Fig. 20. Simulated and measured spherical coverage gain cdf curves of the proposed antenna array at different frequencies.

As shown in Fig. 19, the 2-D total scan patterns are synthesized at 23.5, 27, and 29.5 GHz in MATLAB using measured radiation patterns of the array elements. 3GPP has introduced a standard to evaluate the overall spherical coverage performance using cumulative distribution function (cdf) for randomly oriented mobile devices. The corresponding cdf curves are plotted in Fig. 20 by interpolating and collecting the results shown in the simulated and measured 2-D total scan patterns. The spherical coverage of the proposed antenna array is higher than 4.9 dBi across the entire frequency band at the 50%-tile cdf.

D. Discussion

To highlight the advantages of the proposed design, a comparison with other reconfigurable antennas is summarized in

Table II. In the open literature, there are few studies on frequency-reconfigurable antenna arrays for mm-wave frequency bands. Currently, the scarcity of VDs that can provide continuous variations has led to the predominant use of p-i-n diodes, which can only realize limited working states. Among the key parameters of mm-wave frequency technology, the proposed design exhibits excellent performance with regard to large operating frequency range, small size, dual polarization, and array configuration of beam-forming capability. Furthermore, this antenna array is well-suited for mass production using standard PCB fabrication processes. Each VD is independently controlled in the prototype to prevent all of them from being broken down together. We believe that the employed feeding network and biasing network can be redesigned for easy integration with IC in the bottom of the array structure so that the antenna array occupies limited space in practical mobile devices.

IV. Conclusion

In this article, a dual-polarized frequency-reconfigurable antenna array is proposed and validated for use in mobile devices working at mm-wave frequency band. The array employs patch antenna elements loaded with VDs. Due to the scarcity of available varactors, series parallel plate capacitors are introduced to reduce the total capacitance and achieve the desired capacitance variations. The antenna efficiency is increased by placing inductive shorting vias close to the corners of the patch. Moreover, the bias circuits of varactors are implemented through features of the antenna structure. As the varactor capacitance varies from 0.22 to 0.033 pF, the proposed design is able to cover a frequency band from 23.2 to 30.2 GHz with a total efficiency greater than -2.5 dB. The spherical coverage gains at the 50%-tile cdf are larger than 4.9 dBi over the entire frequency band. Furthermore, stable performance is maintained when the four-element antenna array is put into a 21×4.5 mm^2 cavity. In the further work, we aim to study the frequency tunability of the proposed antenna array by expanding the covered frequency bands. For example, p-i-n diodes can be employed to switch between two working frequency ranges: the low band (24–29.5 GHz) and high band (37–43.5 GHz). The proposed approach presents new possibilities for designing frequency-reconfigurable antennas for 5G handsets operating in mm-wave frequency bands.

References

[1] Z. Ying, "Antennas in cellular phones for mobile communications," *Proc. IEEE*, vol. 100, no. 7, pp. 2286–2296, Jul. 2012.

[2] A. Al-Dulaimi, S. Al-Rubaye, Q. Ni, and E. Sousa, "5G communications race: Pursuit of more capacity triggers LTE in unlicensed band," *IEEE Veh. Technol. Mag.*, vol. 10, no. 1, pp. 43–51, Mar. 2015.

[3] W. Zeng, F. Chen, and Q. Chu, "Bandwidth-enhanced 5G mobile phone antenna pair with tunable electric field null," *IEEE Trans. Antennas Propag.*, vol. 71, no. 2, pp. 1960–1964, Feb. 2023.

[4] J. G. Andrews et al., "What will 5G be?" *IEEE J. Sel. Areas Commun.*, vol. 32, no. 6, pp. 1065–1082, Jun. 2014.

[5] *User Equipment (UE) radio transmission and reception; Part 2: Range 2 Standalone (Release 16)*, Standard 3GPP TS, 2011.

[6] W. Hong, K. Baek, and S. Ko, "Millimeter-wave 5G antennas for smartphones: Overview and experimental demonstration," *IEEE Trans. Antennas Propag.*, vol. 65, no. 12, pp. 6250–6261, Dec. 2017.

[7] M. Stanley, Y. Huang, H. Wang, H. Zhou, Z. Tian, and Q. Xu, "A novel reconfigurable metal rim integrated open slot antenna for octa-band smartphone applications," *IEEE Trans. Antennas Propag.*, vol. 65, no. 7, pp. 3352–3363, Jul. 2017.

[8] Q. Chen et al., "Single ring slot-based antennas for metal-rimmed 4G/5G smartphones," *IEEE Trans. Antennas Propag.*, vol. 67, no. 3, pp. 1476–1487, Mar. 2019.

[9] C. R. White and G. M. Rebeiz, "A differential dual-polarized cavity-backed microstrip patch antenna with independent frequency tuning," *IEEE Trans. Antennas Propag.*, vol. 58, no. 11, pp. 3490–3498, Nov. 2010.

[10] N. Nguyen-Trong and C. Fumeaux, "Tuning range and efficiency optimization of a frequency-reconfigurable patch antenna," *IEEE Antennas Wireless Propag. Lett.*, vol. 17, no. 1, pp. 150–154, Jan. 2018.

[11] J. Hannula, J. Holopainen, and V. Viikari, "Concept for frequency-reconfigurable antenna based on distributed transceivers," *IEEE Antennas Wireless Propag. Lett.*, vol. 16, pp. 764–767, 2017.

[12] K. X. Wang and H. Wong, "A reconfigurable CP/LP antenna with cross-probe feed," *IEEE Antennas Wireless Propag. Lett.*, vol. 16, pp. 669–672, 2017.

[13] W. Duan, X. Y. Zhang, S. Liao, K. X. Wang, and Q. Xue, "Multiport power combining patch antenna with stable reflection coefficient and radiation pattern in six polarization states," *IEEE Trans. Antennas Propag.*, vol. 67, no. 2, pp. 719–729, Feb. 2019.

[14] M. Tang, Y. Duan, Z. Wu, X. Chen, M. Li, and R. W. Ziolkowski, "Pattern reconfigurable, vertically polarized, low-profile, compact, near-field resonant parasitic antenna," *IEEE Trans. Antennas Propag.*, vol. 67, no. 3, pp. 1467–1475, Mar. 2019.

[15] Y. Juan, W. Che, W. Yang, and Z. N. Chen, "Compact pattern-reconfigurable monopole antenna using parasitic strips," *IEEE Antennas Wireless Propag. Lett.*, vol. 16, pp. 557–560, 2017.

[16] L. Ge, Y. Li, J. Wang, and C. Sim, "A low-profile reconfigurable cavity-backed slot antenna with frequency, polarization, and radiation pattern agility," *IEEE Trans. Antennas Propag.*, vol. 65, no. 5, pp. 2182–2189, May 2017.

[17] G. Yang, J. Li, B. Cao, D. Wei, S. Zhou, and J. Deng, "A compact reconfigurable microstrip antenna with multidirectional beam and multipolarization," *IEEE Trans. Antennas Propag.*, vol. 67, no. 2, pp. 1358–1363, Feb. 2019.

[18] J. Zhang, S. Zhang, Z. Ying, A. S. Morris, and G. F. Pedersen, "Radiation-pattern reconfigurable phased array with p-i-n diodes controlled for 5G mobile terminals," *IEEE Trans. Microw. Theory Techn.*, vol. 68, no. 3, pp. 1103–1117, Mar. 2020.

[19] C. Fan, B. Wu, Y. Hu, Y. Zhao, and T. Su, "Millimeter-wave pattern reconfigurable Vivaldi antenna using tunable resistor based on graphene," *IEEE Trans. Antennas Propag.*, vol. 68, no. 6, pp. 4939–4943, Jun. 2020.

[20] E. Al Abbas, N. Nguyen-Trong, A. T. Mobashsher, and A. M. Abbosh, "Polarization-reconfigurable antenna array for millimeter-wave 5G," *IEEE Access*, vol. 7, pp. 131214–131220, 2019.

[21] J. Park, M. Choo, S. Jung, D. Choi, J. Choi, and W. Hong, "A software-programmable directivity, beamsteering, and polarization reconfigurable block cell antenna concept for millimeter-wave 5G phased-array architectures," *IEEE Trans. Antennas Propag.*, vol. 69, no. 1, pp. 146–154, Jan. 2021.

[22] J. Choi et al., "Frequency-adjustable planar folded slot antenna using fully integrated multithrow function for 5G mobile devices at millimeter-wave spectrum," *IEEE Trans. Microw. Theory Techn.*, vol. 68, no. 5, pp. 1872–1881, May 2020.

[23] M. Patriotis, F. N. Ayoub, Y. Tawk, J. Costantine, and C. G. Christodoulou, "A compact active Ka-band filtenna for CubeSats," *IEEE Antennas Wireless Propag. Lett.*, vol. 20, no. 11, pp. 2095–2099, Nov. 2021.

[24] J. Kim and J. Oh, "Liquid-crystal-embedded aperture-coupled microstrip antenna for 5G applications," *IEEE Antennas Wireless Propag. Lett.*, vol. 19, no. 11, pp. 1958–1962, Nov. 2020.

[25] I. F. da Costa, A. Cerqueira S., D. H. Spadoti, L. G. da Silva, J. A. J. Ribeiro, and S. E. Barbin, "Optically controlled reconfigurable antenna array for mm-wave applications," *IEEE Antennas Wireless Propag. Lett.*, vol. 16, pp. 2142–2145, 2017.

[26] B. Ghassemiparvin and N. Ghalichechian, "Paraffin-based RF microsystems for millimeter-wave reconfigurable antenna," *IEEE Trans. Antennas Propag.*, vol. 70, no. 1, pp. 744–749, Jan. 2022.

[27] Q. Chen, J. Ala-Laurinaho, A. Khripkov, J. Ilvonen, R. M. Moreno, and V. Viikari, "Dual-polarized patch antenna of large frequency tuning range at mm-wave frequency bands," in *Proc. 17th Eur. Conf. Antennas Propag. (EuCAP)*, Mar. 2023, pp. 1–3.

[28] *Solderable GAAs Constant Gamma Flip-Chip Varactor Diode*. Accessed: May 10, 2022. [Online]. Available: https://www.macom.com/products/product-detail/MAVR-011020-1411.html

[29] D. Rotshild and A. Abramovich, "Realization and validation of continuous tunable metasurface for high resolution beam steering reflector at K-band frequency," *Int. J. RF Microw. Comput.-Aided Eng.*, vol. 31, no. 4, Apr. 2021, Art. no. e22559.

[30] R. B. Waterhouse and N. V. Shuley, "Scan performance of infinite arrays of microstrip patch elements loaded with varactor diodes," *IEEE Trans. Antennas Propag.*, vol. 41, no. 9, pp. 1273–1280, Sep. 1993.

[31] I. Ben Trad, I. Rouissi, J. Floc'h, and H. Trabelsi, "Frequency reconfigurable multiband planar antenna with wide tuning frequency range," in *Proc. 10th Eur. Conf. Antennas Propag. (EuCAP)*, Apr. 2016, pp. 1–4.

[32] R. Garg, P. Bhartia, I. J. Bahl, and A. Ittipiboon, *Microstrip Antenna Design Handbook*. Boston, MA, USA: Artech House, 2001.

Quangang Chen was born in Henan, China, in 1992. He received the B.S. degree in electronic information engineering and the M.S. degree in electromagnetic field and microwave technology from the Nanjing University of Science and Technology, Nanjing, China, in 2015 and 2018, respectively. He is currently pursuing the Ph.D. degree with the Department of Electronics and Nanoengineering, School of Electrical Engineering, Aalto University, Espoo, Finland.

From 2018 to 2019, he was a Research Assistant with the College of Electronic Science and Technology, Shenzhen University, Shenzhen, China. His current research interests include sub-6 GHz and mm-wave antennas for mobile devices.

Juha Ala-Laurinaho received the Diploma Engineer (M.Sc.) degree in mathematics and the D.Sc. (Tech.) degree in electrical engineering from the TKK Helsinki University of Technology, Espoo, Finland, in 1995 and 2001, respectively.

He was with Aalto University (formerly TKK), Espoo, where he was also with the Radio Laboratory from 1995 to 2007, and the Department of Radio Science and Engineering from 2008 to 2016, and is currently with the Department of Electronics and Nanoengineering. He is also working as a Staff Scientist. He has been a Researcher and Project Manager in various millimeter-wave-technology-related projects. His current research interests include antennas and antenna measurement techniques for millimeter and submillimeter waves, and the millimeter wave imaging.

Alexander Khripkov (Member, IEEE) received the B.S. degree in radio engineering and the Ph.D. degree in antennas and microwave devices from the Southern Federal University of Russia, Rostov-on-Don, Russia, in 2002 and 2007, respectively.

From 2007 to 2012, he was a Researcher with the Department of Ultrawide Band Sensors for Medical Applications, Industrial Technology Research Institute, Hsinchu, Taiwan. From 2012 to 2016, he was a Group Leader of the Electromagnetic Solutions Group, Samsung Research and Development Institute, Moscow, Russia. He is currently a Principal Antenna Engineer with the Terminal Antenna and RF Laboratory, Huawei Technologies Finland, Helsinki, Finland. He has authored or coauthored about 30 articles in peer-reviewed journals and conference proceedings, and holds over 20 granted U.S. patents and over 50 granted patents in other countries. His current research interests include reconfigurable microwave/millimeter-wave MIMO antenna arrays and circuits, technologies for beyond 5G–6G telecommunication systems, MIMO imaging radars, and metamaterial-inspired structures.

Dr. Khripkov was a recipient of over ten industrial awards.

Janne Ilvonen was born in Helsinki, Finland, in 1976. He received the M.Sc. and Lic.Sc. degrees (Hons.) and the D.Sc. (Tech.) degree in electrical engineering from Aalto University, Espoo, Finland, in 2009, 2012, and 2014, respectively.

From 2015 to 2016, he was a Senior Antenna Engineer with Microsoft Mobile, Espoo, where he was developing antenna concepts for Microsoft's future flagship handsets. Since 2016, he has been with Huawei Technologies Finland, Helsinki, Finland, as a Principal Antenna Engineer. His current research interests include sub-6 GHz and mm-wave 5G handset antennas.

Resti Montoya Moreno was born in Albacete, Spain, in 1992. He received the B.Sc. (Tech.) degree in telecommunications engineering from the Universitat Politécnica de Valéncia, Valéncia, Spain, in 2014, and the M.Sc. (Tech.) and D.Sc. (Tech.) degrees in electrical engineering from Aalto University, Espoo, Finland, in 2016 and 2020 respectively.

He joined Intel as an RF Engineer Intern in 2016. Since 2020, he has been a Senior Antenna Engineer for Huawei Technologies Finland, Helsinki, Finland. His current research interests include 5G and mm-wave antennas for base stations and mobile devices.

Ville Viikari (Senior Member, IEEE) received the Master of Science (Tech.) and Doctor of Science (Tech.) (Hons.) degrees in electrical engineering from the Helsinki University of Technology (TKK), Espoo, Finland, in 2004 and 2007, respectively.

From 2001 to 2007, he was with the Radio Laboratory, TKK (now part of Aalto University), where he studied antenna measurement techniques at submillimeter wavelengths and antenna pattern correction techniques. From 2007 to 2012, he was a Research Scientist and a Senior Scientist with the VTT Technical Research Center, Espoo, where his research included wireless sensors, RFID, radar applications, MEMS, and microwave sensors. He was appointed as an Assistant Professor at Aalto University, Espoo, Finland, in 2012. He is currently a Professor and the Deputy Head of Department with the School of Electrical Engineering, Aalto University. He has authored or coauthored more than 90 journal articles and 100 conference papers. He is an inventor of 16 granted patents. His current research interests include antennas for mobile devices and networks, antenna clusters and coupled arrays, RF-powered devices, and antenna measurement techniques.

Dr. Viikari is a Regional Delegate of EurAAP. He was a recipient of the Young Researcher Award of the Year 2014, presented by the Finnish Foundation for Technology Promotion, and the IEEE Sensors Council 2010 Early Career Gold Award.